Multiphase flow patterns in entrained-flow slagging gasifiers: physical modelling of particle-wall impact at near-ambient conditions

Maurizio Troiano[a], Roberto Solimene[b,*], Piero Salatino[a], Fabio Montagnaro[c]

[a] *Dipartimento di Ingegneria Chimica, dei Materiali e della Produzione Industriale, Università degli Studi di Napoli Federico II, Piazzale Vincenzo Tecchio 80, 80125 Napoli (Italy).*

[b] *Istituto di Ricerche sulla Combustione, Consiglio Nazionale delle Ricerche, Piazzale Vincenzo Tecchio 80, 80125 Napoli (Italy).*

[c] *Dipartimento di Scienze Chimiche, Università degli Studi di Napoli Federico II, Complesso Universitario di Monte Sant'Angelo, 80126 Napoli (Italy).*

Abstract.

Particle–wall interaction phenomena relevant to multiphase flow in entrained-flow slagging coal gasifiers have been investigated. The micromechanical patterns of particle impingement on the reactor walls have been characterized in a model system by high speed imaging and tracking of wax particles impacted onto a flat surface at near-ambient conditions. The solid/plastic versus fluid state of the wax particles was controlled by proper selection of the particle, ambient and target temperatures. Particle–wall collision was described in terms of normal and lateral restitution coefficients and capture efficiency. The influence of the particle stickiness, impact velocity and angle, and surface properties and structure of the target on the rebound patterns was studied. Results indicate that the elastic–plastic adhesive model provides an adequate representation of the non sticky particle–wall collisions. Moreover, the presence of a powder layer on the target favours energy dissipation and accumulation of particles close to the surface. This pattern promotes the establishment of a dense-dispersed phase in the near-wall zone of entrained-flow slagging gasifiers. Increasing the temperature, particles shift from the solid/plastic to the fluid state and the coefficient of restitution drops to vanishingly small values, confirming that deposition is the prevailing phenomenon during the collision of sticky particles on a wall.

Keywords: particle–wall interaction; entrained flow; slagging gasifiers; cold impact test; restitution coefficient.

* Corresponding author. T: +39 081 7682248. F: +39 081 5936936. E: solimene@irc.cnr.it.

1. Introduction.

Entrained-flow gasification (EFG) keeps an important role in the current portfolio of solid fuel conversion technologies. EFG outperforms most competing technologies from the standpoints of overall energy conversion efficiency and emission control. Moreover it provides adaptive and flexible routes toward integration of energy conversion with fuel and chemical synthesis and/or CO_2 capture.

Entrained-flow gasifiers are characterized by short residence times (in the order of a few seconds), hence, very fine particle sizes and high temperatures are required to allow a good conversion. High temperatures ensure the destruction of tars. Unburnt carbon is vanishingly small if the time-temperature history of the fuel particles and oxidizing/reducing conditions are properly tuned by careful control of multiphase flow in the gasification chamber. Most industrial EF gasifiers operate in the slagging mode: fuel particles migrate toward the reactor walls, mainly due to swirled/tangential flow and "turbophoresis" promoted in the reaction chamber. Bulk-to-wall migration of solids results, thanks to the very high operating temperatures, into the build-up of a slag layer of molten ash, which flows along the reactor internal walls and is eventually drained at the bottom of the gasification chamber [1–6].

The performance of slagging EF gasifiers may be critically affected by the fate of char/ash particles as they interact with the wall slag layer [7–10]. Montagnaro and Salatino [11] developed a phenomenological model, which considers the establishment of a particle segregated phase in the near-wall region of the gasifier. Char particles impinging on the wall slag layer can either be entrapped inside the melt, or adhere onto the slag layer's surface. The first scenario is unlikely to occur, on the basis of forces and energy balances governing char/slag interaction [7,11], along with particle impact velocities and trajectories throughout the gasifier [12]. On the other hand, if particles adhere onto the slag layer's surface, further carbon conversion is possible. When the slag layer is extensively covered by char particles, further entrapment of particles is prevented, and a densely dispersed segregated particle cloud may establish in the close proximity of the wall ash layer. This annular phase moves slower than the lean particle-laden gas phase, hence, particles residence times in this region are longer than the average gas space-time. This feature is responsible for enhanced carbon conversion. The soundness of this phenomenological framework has been confirmed by experimental and theoretical studies [13–15].

Particle–wall interaction occurs according to different micromechanical patterns, which depend on parameters such as particle and wall temperatures, solid/molten status of the particles and wall layer, char conversion degree, particle kinetic energy, surface tension of the slag layer, particle effective stiffness and char/slag interfacial tension [8,10,11,16]. Char–slag interaction patterns are hereby classified on the basis of the *stickiness degree* of the wall layer and of the impinging char particle:

- the material laying on the wall (prevailingly, inorganic ash) is *sticky* when the wall temperature is high enough to ensure an ash molten status, generating a liquid slag layer. An additional condition for the slag layer to be sticky is that it must not be extensively covered by *non sticky* char particles;
- the char particle is sticky when its temperature is beyond the ash melting point, and its carbon conversion degree is beyond a given threshold value, as the plastic behaviour is emphasized when the carbon content, which is inherently refractory, is reduced.

On the basis of this classification, four interaction scenarios establishing during EF gasification can be considered, namely: *(i)* non sticky char/ash particle impinging on a molten-slag-covered sticky wall (*NSP–SW*); *(ii)* non sticky char/ash particles impinging on a non sticky wall (*NSP–NSW*); *(iii)* molten, i.e. sticky, ash particles impinging on a non sticky wall (*SP–NSW*); *(iv)* molten sticky ash particles impinging on a sticky wall (*SP–SW*).

Mechanistic understanding of particle–wall interactions in EF systems for *SP–SW* and *NSP–NSW* regimes has been recently undertaken by Troiano et al. [17,18], using the tool of physical modeling. They investigated the particle–wall interactions in a lab-scale cold EF reactor, equipped with a nozzle, whence molten wax could be atomized into a mainstream of air. Operating temperatures were adjusted so as to tune the sticky–non sticky behaviour of both impinging wax droplets and wall layer. Furthermore, both laminar and turbulent gas flow conditions were applied. The assessment of flow and segregation patterns was obtained by the selective collection of wax at the exhaust of the reactor, and by image analysis and particle tracking. Their findings confirmed that particle deposition and segregation are enhanced by particle stickiness and turbulence.

The relationship between particle deposition and slagging has been extensively addressed in previous studies. According to Baxter [19,20], ash deposition rate under inertial conditions is proportional

to the particle capture efficiency, which in turn depends on ash stickiness and the properties of the surface against which particles are impacted. For synthetic and alkali-rich ash, the stickiness criterion is verified when the weight fraction of the liquid phase in the particle is nearly 15% [21,22]. Bool and Johnson [23] studied the ash deposition behaviour during coal combustion in an EF reactor. Ash collection efficiencies on a deposition probe sharply increased to a maximum as char burnout approached a critical value, to slightly decrease thereafter. This result confirms that the effective ash stickiness depends on its residual carbon content. Furthermore, the sharp rise in the stickiness indicates a change in the structure of the particles around the critical char burnout, from porous and non sticky char, to molten sticky slag. Whitty and co-workers [24] studied the transition from char to slag for a bituminous coal using a laminar EF reactor under oxidizing conditions. In the initial stage of coal oxidation (the initial stage of char–slag transition), minerals are still encapsulated in the residual refractory carbon matrix, and the char particle is non sticky. At intermediate to large particle conversion (the middle stage of the transition), encapsulated minerals begin to appear on the external surface of the char and they melt, increasing the effective stickiness of the char particle. At even larger particle conversion (the final stage of the transition), the included minerals are released, forming molten slag. This char–slag transition occurs at a conversion degree $X_C \approx 90\%$ [24], provided that the temperature exceeds the ash melting point.

Several empirical methods, for instance slagging indices, ash sticking temperatures and viscosity models, were proposed in the literature to determine particle sticking criteria [25–27]. The modified "Urbain Model" is widely used to model the viscosity of coal ash on the basis of the acid-to-base ratio and can be coupled with other criteria to determine the fate of char particles in entrained-flow reactors [26]. The temperature at which the amorphous slag transforms into a crystalline phase is used to calculate the critical viscosity. Therefore, for particle viscosity lower than the critical value (namely, at higher temperatures), the particle sticks. The drawback of these viscosity models to predict particle sticking is that they do not take into account the effect of residual carbon on particle stickiness and the stickiness of the target wall. The modified "Urbain Model" can be coupled with other criteria to describe the behaviour of char/slag interaction in entrained-flow reactors [16,28].

The fate of char/ash particles in the near-wall region of EFG is better predicted by detailed

mathematical and physical modelling. Particle–wall interactions can be investigated and described in terms of a coefficient of restitution (the ratio between the rebound and the impact velocities). Dong et al. [29] investigated the normal restitution coefficient of fly ash particles impacting on a planar surface at room temperature. Pisupati and co-workers [30] carried out EF and drop experiments at ambient conditions to simulate the different particle–surface collision patterns relevant to EFG. The restitution coefficient is an important parameter when modelling multiphase flow in the gasification chamber, e.g. by the tools of CFD-DPM, as it critically affects the boundary condition for particle−wall collisions.

The aim of the present study is the characterization of the coefficient of restitution during impact experiments of particles at different stages between solid/plastic to fluid conditions. Despite targeted at characterizing the dynamics of particle–wall interaction in EF slagging gasifiers, a physical modelling approach was followed, by simulating the real process with synthetic wax particles impacted against a target at near-ambient conditions. The influence of the stickiness of the particles and of the target surface, of the impact velocity, of the impact angle as well as of the material and structure of the target were investigated.

2. Theoretical background of particle–wall collision.

Particle–wall collisions are generally characterized in terms of a restitution coefficient ε, defined as the ratio between the rebound and the impact velocity. The coefficient takes the value ε=1 when the impact is perfectly elastic, whereas $\varepsilon \to 0$ when the particles dissipate all their kinetic energy at the impact and adhere on the surface. The restitution coefficient embodies phenomena like elasto–plastic deformation and viscoelastic behaviour (energy loss due to wave propagation) of solid materials, surface contact forces and particle–wall friction. Different particle−wall impact models are reported in literature [31–35]. Among them, the model developed by Thornton and Ning [36] seems to be sufficiently accurate to describe the normal impact of fine particles, such as fly ash, onto a planar surface, as reported by Dong et al. [29]. This model takes into account adhesion effects during the normal impact of elastic−perfectly plastic spheres. In their model, the normal restitution coefficient is zero at impact velocities lower than a threshold value: the particles adhere on the surface as the impact energy is smaller than the adhesion energy [33].

This critical velocity, also called “capture” or “sticking” velocity, v_s, is a function of particle size and density, particle surface energy and elastic properties of both the particle and surface (Young’s moduli and Poisson’s ratios) [36], as follows:

$$v_s = 1.84\left[\frac{4\left(\frac{2\Gamma}{d_p}\right)^5}{3\rho_p^3 K^2}\right]^{\frac{1}{6}} \quad (1)$$

where Γ is the surface energy at the interface, d_P and ρ_P are the particle diameter and density, respectively, and K is the composite Young’s modulus, expressed as:

$$K = \frac{4}{3}\left(\frac{1-\nu_1^2}{E_1} + \frac{1-\nu_2^2}{E_2}\right)^{-1} \quad (2)$$

where E_1 and E_2 are the Young’s moduli, and ν_1 and ν_2 are the Poisson’s ratios, for the particle and the surface, respectively.

Particles with impact velocities larger than the sticking velocity rebound for elastic impact and in certain cases of elastic–plastic impact [36]. For elastic materials, the normal restitution coefficient approaches 1, whereas for elastic–plastic materials the restitution coefficient increases with the impact velocity, as far as the material displays elastic behaviour. When the impact velocity is further increased, plastic deformation begins, inducing additional energy losses during the impact, and a decrease in the value of the normal restitution coefficient. The limiting velocity above which plastic deformation occurs is called “yielding velocity” v_y, and it is determined by the bulk properties of the particles and the wall, while it is independent of the particle size [33,36,37]:

$$v_y = \left(\frac{2\pi}{3K}\right)^2\left(\frac{2}{5\rho_p}\right)^{\frac{1}{2}} p_y^{\frac{5}{2}} \quad (3)$$

where p_y is the limiting contact pressure at which the first irreversible deformation occurs (also called "cut-off pressure"). It depends on both the impact parameters (velocity) and the particle mechanical properties (yield strength).

Thornton and Ning [36] derived an analytical solution for the coefficient of restitution for normal impacts of adhesive, elastic–perfectly plastic spheres, expressed in terms of the impact, capture and yielding velocities (v_i, v_s and v_y, respectively):

$$\varepsilon_n = 0 \qquad \text{for } v_i \le v_s \tag{4}$$

$$\varepsilon_n = \left[1 - \left(\frac{v_s}{v_i}\right)^2\right]^{\frac{1}{2}} \qquad \text{for } v_s \le v_i \le v_y \tag{5}$$

$$\varepsilon_n^2 = \frac{6\sqrt{3}}{5}\left[1 - \frac{1}{6}\left(\frac{v_y}{v_i}\right)^2\right]\left[\frac{\frac{v_y}{v_i}}{\frac{v_y}{v_i}+2\sqrt{\frac{6}{5}-\frac{1}{5}\left(\frac{v_y}{v_i}\right)^2}}\right]^{\frac{1}{2}} - \left(\frac{v_s}{v_i}\right)^2 \qquad \text{for } v_i \ge v_y \tag{6}$$

When an oblique impact is considered, the particle–wall friction expressed by the tangential restitution coefficient must be taken into account, too [38–41]. Moreover, particle rolling and sliding may occur on the verge of the impact. Figure 1 shows a particle impacting and bouncing off a flat surface with its velocity components and angles. It is useful to define a normal and a tangential coefficient of restitution, ε_n and ε_t, respectively, as:

$$\varepsilon_n = \frac{-v_{n,r}}{v_{n,i}} \tag{7}$$

$$\varepsilon_t = \frac{v_{t,r}}{v_{t,i}} \tag{8}$$

where $v_{n,i}$ and $v_{n,r}$ are the normal components of the impact and rebound velocity, respectively, and $v_{t,i}$ and $v_{t,r}$ are the corresponding tangential components. It is also possible to define a global coefficient of restitution ε_g as:

$$\varepsilon_g = \frac{v_r}{v_i} = \sqrt{\frac{v_{n,r}^2}{\frac{v_{n,i}^2}{sin^2\,\alpha_i}} + \frac{v_{t,r}^2}{\frac{v_{t,i}^2}{cos^2\,\alpha_i}}} = \sqrt{\varepsilon_n^2\,sin^2\,\alpha_i + \varepsilon_t^2\,cos^2\,\alpha_i} \tag{9}$$

where ε_g tends to ε_n for large impact angles ($\alpha_i \to 90°$) and to ε_t for small impact angles ($\alpha_i \to 0°$). The particle rebound behaviour is deeply influenced by the impact angle. According to the rigid body theory, a sphere slides at small impact angles and rolls at near-normal angles as it impacts against a planar target. When sliding occurs throughout the impact, the tangential coefficient of restitution can be expressed as a function of ε_n, α_i and of the tangential-to-normal impulse ratio f [39–41], as:

$$\varepsilon_t = 1 - f(1 + \varepsilon_n)\tan\alpha_i \tag{10}$$

The critical impact angle at which the transition from sliding to rolling occurs can be expressed as [41]:

$$\alpha_i^{cr} = \cot^{-1}\left[\frac{7k-1}{k}\frac{f}{2}(1 + \varepsilon_n)\right] \tag{11}$$

where k is the ratio of the tangential to the normal composite stiffness [42]:

$$k = \frac{\frac{1-\nu_1}{G_1} + \frac{1-\nu_2}{G_2}}{\frac{1-\frac{\nu_1}{2}}{G_1} + \frac{1-\frac{\nu_2}{2}}{G_2}} \tag{12}$$

G_1 and G_2 being the shear modulus for the particle and the surface, respectively.

3. Experimental.

3.1. Materials and experimental apparatus.

The rebound behaviour of the char/ash particles and of the slag layer has been simulated, at nearly ambient conditions, by wax particles. Waradur E (Völpker Spezialprodukte, Germany) was selected, as the rheological/mechanical properties of this wax (a refined material made from black raw montan wax) resembled, under molten state, those of a typical coal slag and, under solid state, those of char particles. The melting range of the wax is 75–85°C, and its viscosity varies in the range 0.02–0.1 kg m^{-1} s^{-1}, as the temperature ranges between 130°C and 90°C [43]. The wax density is around 1000 kg m^{-3}. Accordingly, the kinematic viscosity is in the order of 10^{-5}–10^{-4} m^2 s^{-1}, consistent with the values commonly reported in the literature for coal slag (viscosity and density on the order of 0.01–1 kg m^{-1} s^{-1} and 2500–3000 kg m^{-3}, respectively, in the temperature range 1200–1500°C) [3,4,7]. The values of the kinematic viscosity of the wax are such to reproduce the laminar flow of the molten phase along the reactor walls, as experienced during the operation of full-scale EF slagging gasifiers. Besides, even if the wax surface tension (0.03 kg s^{-2} at 100°C) is lower than that typical of slag (0.4–0.7 kg s^{-2} [3]), the wax properties are such that the so-called "entrapment" and "over-layering" criteria are not satisfied, and the segregation or segregation–coverage regimes are likely to be established, as expected for realistic particle–slag interactions in EFG [11,13,17,18]. In order to evaluate the particle rebound characteristics, the wax mechanical properties were determined by uniaxial compressive tests in accordance with ASTM D 695-10, with a dynamometer INSTRON 3360 equipped with a load cell of 10 kN. Seven wax cylindrical samples, 0.025 m-height, were tested. Figure 2 shows a typical stress–strain curve for wax samples. Table 1 reports the mean values of the mechanical properties of the wax and of different coals [44,45], together with their standard deviation. The Young's modulus of slag calculated at high temperatures [46] has also been reported for comparison. The mechanical properties of the wax agree quite well with data reported in Table 1.

Particle–wall micromechanical interactions were investigated by means of the experimental apparatus reported in Figure 3. The test rig consisted of a vertical Pyrex tube, 0.65 m-height and 0.03 m-ID, connected at the top with another Pyrex tube (0.01 m-ID and 0.013 m-OD) running coaxially for 0.08 m inside the larger tube. Batches of wax microparticles (50–100 μm) were fed into the smaller tube by means

of a Pasteur pipette. Air was fed sideways at the top of the tube, and flowed downward between the inner and outer tubes. The particles flowed through the inner tube driven by gravity, and then in the outer tube where they were entrained by the air flow. The particle impact velocity was controlled regulating the air flow rate Q_a, by means of a flow meter/controller (Bronkhorst High-Tech). The temperature T_a of the air stream could be adjusted by means of a temperature controller. When the particles exited the tube, they impacted on a target plate placed around 0.05 m below the bottom end of the tube. The target could be inclined to obtain particle impact angles ranging from about 5° to about 90° with respect to the horizontal. The tube length L was chosen on the basis of the particle relaxation time τ and of the particle impact velocity. Typical values of particle impact velocity in EFG are on the order of 2 m s^{-1} [7]. In order to approach similar velocities, the length L of the eductor tube was calculated from the relationship:

$$L = 10\tau v_i = 10\frac{\rho_p d_p^2}{18\mu} v_i \tag{13}$$

where μ is the fluid viscosity, and the particle relaxation time was conservatively multiplied by 10. For the typical values of operational parameters, Eq. (13) gave L=0.65 m. Furthermore, the tube length was such that the particle residence time was about three times longer than the characteristic fusion time of the wax (about 0.11 s for a 100 µm-particle). This feature enabled the characterization of the impact dynamics of wax particles at different temperatures, i.e. with different stickiness degrees (from *NSP* to *SP*). The particle impact velocity was calculated as the sum of the gas velocity in the tube and the particle terminal velocity, and it was experimentally verified by particle tracking at the exit of the tube with a high-speed video camera (Photron Ultima APX). Particle velocities before and after the impact were determined experimentally, hence the restitution coefficient was calculated.

Four different target materials were used, in order to investigate the effect of the particle/wall interfacial energy on the rebound characteristics: Pyrex, stainless steel, montan wax Waradur E and Teflon. The targets surface energies are reported in Table 2. In particular, the wax target was obtained by solidification of melted wax, in order to have a smooth surface.

Additional experimental impact tests were carried out after the target surface (either dry or wet) was layered with wax powder (d_p=75±10 μm) of different thickness (between about 0.2 mm and 1.4 mm) and voidage around 0.5. These experiments aimed at simulating the rebound behaviour of a particle hitting adhered particles covering either a dry refractory wall or the slag layer (*NSP–NSW* regime for both cases). For this kind of tests, the dry wall was represented by the Pyrex target, while the liquid layer was represented by a syrup (μ_{syr}=0.5–1 Pa s @25°C, ρ_{syr}=1280 kg m^{-3}, γ_{syr}=0.05 N m^{-1}) to mimic the slag layer at ambient conditions.

3.2. Operating conditions.

Batches of spherical wax particles were used. They were obtained by previous melting, atomization and solidification in another lab-scale experimental apparatus, presented elsewhere [17,18]. A SEM micrograph of a sample of the wax particles used during the experimental campaign is reported in Figure 3. The experimental tests aimed at characterizing the phenomenology of particle–wall interaction from a micromechanical point of view, in terms of restitution coefficients and capture efficiency. In particular, *NSP–NSW* regime, *SP–NSW* regime and the transition from the two regimes were investigated by varying different operating parameters, as reported in Table 3. Experiments probed the influence of: *(i)* increasing air temperature, which enabled to switch from non-sticky to sticky particle conditions; *(ii)* the target material and the target structures, used for the investigation of the *NSP–NSW* regime.

Snapshots of particle/droplet impacts were taken with a progressive scan CCD camera (Photron Ultima APX), equipped with a magnifying zoom lens and a 27.5 mm extension tube. The camera head (CMOS 10 bit-monochrome) was connected to a processor, which stored non-compressed digital data of high-speed recorded images. The processor was connected to a personal computer, where it was possible to visualize and save the downloaded images. Frame-by-frame recording was accomplished at a sampling rate of 1000 fps, with a 0.028 m × 0.028 m recording window digitized as 1024 × 1024 square pixels (spatial resolution of about 27 μm), while the shutter time was set to 42 μs. Furthermore, a halogen lamp (Osram 800 W, 3200 K), a white paperboard as reflecting and diffusing surface, and a black paperboard as

background were used to achieve proper lighting of the impact zone. Each recorded frame was post-processed using the program Image-Pro Plus. In particular, it was possible to identify the position of each particle in the x and y directions. The particle incident and rebound velocities in the x and y directions were calculated based on the frame rate and the particle distance travelled between two consecutive frames before and after the impact, respectively. Impact and rebound angles were measured from the particle position before and after a collision. All the experimental results were then grouped and classified by velocity, size, temperature and impact angle ranges, by means of an algorithm developed in Matlab language and environment. A sample of the measurements is given in Figure 4, reporting a wax particle (d_p=70 μm) as it collides and bounces off the Pyrex target at room temperature (*NSP–NSW* regime). The time-series of the particle dimensionless coordinates, x^* and y^*, during impact and rebound are reported in Figure 5, where $x^* = x(t)/x^0$ and $y^* = y(t)/y^0$. $x(t)$, $y(t)$ and x^0, y^0 are the coordinates of the particle center at time t and at time t=0, respectively. In Figure 5, the star (black/white) symbol represents the closest position of the particle to the target (t=4 ms, see Figure 4). The coordinate x^* linearly increases with time before and after collision, as the particle moves from the left to the right. The different slope before and after the impact means that the value of the tangential coefficient of restitution is not equal to 1. Also y^* has a linear dependence on time before and after collision, decreasing during the impact phase and increases during the rebound phase. The distance travelled by the particle in the y direction during the rebound phase is shorter than that recorded during the impact phase, and this is a first indication that the normal restitution coefficient is smaller than 1.

In this work, the rebound characteristics for the *NSP–NSW* regime were expressed in terms of restitution coefficients, while for the *SP–NSW* regime they were expressed in terms of capture efficiency $(C.E.)$, defined as the fractional number of adhered particles over the number of total impacted particles:

$$C.E. = \frac{N_p^{\varepsilon_g=0}}{N_p^{tot}} 100\% \tag{14}$$

Finally, for the transitional *NSP→SP* regimes, both restitution coefficients and capture efficiency were measured.

4. Results and discussion.

The experimental results included (cf. also Table 3): the restitution coefficients of wax particles colliding against the target surface in the *NSP–NSW* regime (operated at 20°C), while varying the impact velocity (from 0.5 to 3 m s^{-1}) and angle (from 10° to 90°) and for different target material and structure *(Section 4.1)*; the restitution coefficients and capture efficiencies of wax particles colliding against the Pyrex target during the transition from the *NSP–NSW* to the *SP–NSW* regime, while varying the particle impact temperature (from 20° to 110°C) whereas the impact velocity and angle were kept at 2 m s^{-1} and 84°, respectively *(Section 4.2)*; the capture efficiency of wax droplets colliding against the Pyrex target in the *SP–NSW* regime (operated at 120°C), while varying the impact velocity (from 0.7 to 5 m s^{-1}) and angle (from 15° to 90°) *(Section 4.3)*. Experimental data for the coefficients of restitution are reported as values averaged over multiple tests (symbols). Bars corresponding to the standard error are also reported. In order to ensure experimental reproducibility, each point is the average of at least 50 measurements.

4.1. Rebound characteristics in the NSP–NSW regime.

Figure 6 reports the effect of the impact angle α_i on the restitution coefficients, for wax particles in the size range 75$\pm$10 µm keeping constant the normal impact velocity, $v_{n.i}$, at a value of 1$\pm$0.1 m s^{-1} (i.e. reducing α_i the particle velocity was increased proportionally to the inverse of $\sin\alpha_i$). The experimental data points show a slight effect of the impact angle on the normal restitution coefficient. The largest value was obtained at small impact angle (ε_n around 0.41 when α_i=35°), while the smallest value corresponds to near-normal impact angle (ε_n around 0.28). These values indicate that the rebound behaviour is plastic, as the restitution coefficients are well below 1. The effect of the impact angle on ε_n has been discussed in several studies. Broom [47] found a 5–10% increase of the normal coefficient of restitution while varying the impact angle from 0° to 45° for the impact of 11 µm-glass particles on an aluminium surface. However, for finer glass particles, 8.6 and 4.7 µm, the trend was opposite. Other researchers [39,48] concluded that

ε_n is nearly constant over the full range of impact angles tested, 0°<α_i<90°. Sommerfeld and Huber [49] reported that the normal coefficient of restitution is larger for small impact angles, while it approaches an almost constant value for large angles. This effect may be caused by a slight non-sphericity or surface degradation of the particles and, probably, by some residual wavy structures on the wall. In the present work, it is likely that ε_n is nearly constant with α_i if the hydrodynamic effect of the air flow is taken into account. The air flow rate used to impact particles ($v_{n,i}$=1 m s^{-1}) at small impact angles was around 4-times larger than that used for normal impacts tests. This could enhance particles lift from the surface at glancing impacts. This aspect is a disadvantage for the accuracy of the data from a mechanistic point of view, but it represents a more realistic condition when compared to what is likely to happen in an EF gasifier.

The trend of the data points for the tangential restitution coefficient reported in Figure 6 is non monotonic with the impact angle. In particular, it is around 0.8 at 13°, then it decreases to a minimum (for α_i≈40°), to increase thereafter, in agreement with trends reported in the literature [39,40]. As regards the effect of α_i on the global restitution coefficient ε_g (affected by both ε_n and ε_t, see Eq. (9) and Figure 6), ε_g tends to ε_t at small impact angles, and to ε_n at large ones. It is possible to fit the experimental data points with Eq. (9) by considering ε_n and ε_t as constant values. The result of this operation is shown in Figure 6, as well. The qualitative trend of the theoretical ε_g agrees fairly well with the experimental data points. The best fit was obtained for ε_n=0.31 and ε_t=0.76.

The variations of ε_t with α_i in Figure 6 can be attributed to the changing history of sliding (at small impact angles) and rolling (at large impact angles) regimes, as the impact angle is varied. The experimental apparatus did not permit to accurately mark the particles to measure the rotational speed before and after the collisions (i.e. rolling motion), while it allowed to characterize the sliding regime by means of the tangential coefficient of restitution. If sliding is described by a tangential-to-normal impulse ratio, f, it is possible to derive ε_t from Eq. (10). Figure 7 reports values of ε_t plotted against $(1+\varepsilon_n)\tan\alpha_i$. The measured points from impact angles between 10° and 45° are fitted fairly well by a straight line corresponding to $f = 0.28$, whereas the data points significantly deviate for $(1+\varepsilon_n)\tan\alpha_i$>1.31, corresponding to α_i>45°. This finding is in very good agreement with the rigid body theory, as the critical impact angle for the transition from sliding to rolling regime is α_i^{cr}=43°, according to Eq. (11). It is possible

to conclude that the rigid body theory well describes the measured variation of ε_t during the sliding regime. As regards the tangential restitution coefficient at large impact angles (α_i>α_i^{cr}), the rigid body analysis would suggest ε_t=5/7=0.714, while in Figure 6 ε_t increases up to 0.85 for α_i≈80°. The reason of this discrepancy lies in the fact that the rigid body theory does not take into account the tangential elastic compliance of the surfaces, which, indeed, influences ε_t during a plastic impact [39,42].

Figure 8 shows the trend of ε_n, obtained when testing in *NSP–NSW* regime at different normal impact velocities (d_p=75±10 μm, α_i=84±1°). The experimental data are compared with those obtained by application of the Thornton and Ning model [36] for impact of adhesive elasto−plastic spheres. The values of the mechanical properties and of the critical velocities v_s and v_y are reported in Table 4, with particular reference to the case under investigation (Pyrex target material). It was v_y<v_s; this means that the wax particle plastically deforms for each normal impact velocity investigated, and that the maximum value of ε_n is less than 1. This finding agrees with the experimental results shown in Figure 8 (ε_n∼0.3). It is recalled that under plastic deformation conditions, the dependence of the restitution coefficient on impact velocity is less pronounced, as predicted by Eq. (6). Furthermore, the calculation of v_y and, as a consequence, of ε_n, required the knowledge of the cut-off pressure p_y, which is generally expressed as $p_y = c \times \sigma_y$, where c is a constant (around 2.6–3 for hard-sphere models [50]) and σ_y the yield stress. The impact of wax particles, instead, can be properly described by a soft-sphere model, for which the collision is not instantaneous [51]. The best agreement between experimental data and Thornton and Ning model was obtain for c=0.7. This means that an incipient plastic deformation occurs when the contact pressure exceeds 70% of the yield stress. This results in a damping effect of the normal restitution coefficient at each impact velocity investigated, due to the particles softness [52]. On the basis of the results shown in Figure 8, it can be speculated that a char particle can be seen as a soft particle, too, especially during the pyrolysis and the latest stage of reaction.

The plastic rebound nature is also confirmed by results obtained in the *NSP–NSW* regime using different target materials, characterized (see Table 4) by different mechanical properties, especially in terms of surface energy and elastic modulus. Figure 9 reports the trends of ε_n and ε_g for 75±10 μm

particles colliding against Pyrex, stainless steel, montan wax Waradur E and Teflon targets, at fixed α_i=84±4° and v_i=1.25±0.1 m s^{-1}. It is quite evident that the nature of the substrate material exerts negligible influence on particle rebound. As a matter of fact, when the impact energy far exceeds the adhesion energy, the coefficient of restitution is primarily a function of the energy losses due to plastic deformation, as described by Eqs. (1), (3) and (6). Accordingly, the restitution coefficient decreases with an increasing impact velocity, and it is a function of the yield velocity only [37]. The small difference in ε_n obtained with different targets indicates that the elastic yield limit velocity was the same in each case, consistent with plastic deformation occurring only in the particle. This behaviour agrees with previous investigations, confirming that the target surface energy does not affect the restitution coefficients during plastic impacts [37].

Figures 10 and 11 report the effect of the target surface properties on the normal and global coefficients of restitution, respectively, for different normal impact velocities. Other parameters were d_p=75±10 μm and α_i=84±4°. The Pyrex and smooth wax surfaces are shown as reference, where ε_n and ε_g are about constant with the impact velocity. Moreover, the two figures report results obtained for the Pyrex target covered by: i) two wax powder layers with different thickness; ii) a syrup layer spotted with wax powder. Both ε_n and ε_g decrease in the presence of a powder layer, and they are smaller for a thicker powder layer. In particular, ε_n (Figure 10) has a mean value equal to 0.28 for the Pyrex and smooth wax targets, while it decreases to around 0.1 for the thin powder layer, and to around 0.07 for the thick powder layer. A similar result is obtained for ε_g in Figure 11. These results may be explained by taking into account that the presence of the powder layer leads to a smaller equivalent elastic stiffness of the powder layer/target structure, a longer contact time, and a larger contact area. All these features bring about larger dissipation due to adhesion force, hence smaller restitution coefficient [53]. This applies also when increasing the thickness of the powder layer. Furthermore, the presence of a powder layer can emphasize energy dissipation due to wave propagation during particle–wall impact. It is remarkable that this reduction is the same regardless of whether a dry (Pyrex) or wet (syrup-layered Pyrex) target are used. This finding may be explained on the basis of the fact that the powder layer separates the impinging particles from the

wall substrates, and the particles partially penetrate the powder layer. These phenomena determine energy dissipation, hence smaller coefficients of restitution, as reported in the literature [54,55]. This finding is very relevant to the assessment of the fate of char/ash particles in EF slagging gasifiers. Smaller restitution coefficients as the target is covered by a powder layer promote the establishment of segregation–coverage regimes, with, in turn, may be responsible for the formation of a dense–dispersed phase in the near-wall zone [11].

4.2. Rebound characteristics in the transitional NSP–NSW→SP–NSW regime.

Figure 12 reports the effect of the particle temperature on capture efficiency (d_p=80±15 μm, α_i=84±4° and v_i=2±0.1 m s^{-1}), defined in Eq. (14). Notably, due to the operating conditions in the impactor, the particle temperature could be considered equal to the temperature of the mainstream air. The capture efficiency increased from 0 to 93% when temperature was increased from 20°C to 105°C. Capture efficiency was practically zero at temperatures below 50°C. At these temperatures the montan wax is solid (its melting range is 75−85°C), thus the particles did not adhere on the target surface. Craig et al. [56] measured the temperatures at which 1%, 50%, and 70% flow occurred, for the montan wax. These temperatures were 65°C, 71.1°C and 74.6°C, respectively. This is in agreement with the experimental points reported in Figure 12, where the capture efficiency was around 8% at 70°C, as a consequence of the incipient solid–liquid transition of the wax. As the temperature is increased even further, there is a sharp rise in the capture efficiency, up to 93% at 105°C.

The behaviour of the wax during its solid–liquid transition resembles that occurring during char–slag transition in gasification processes. To better appreciate this, the capture efficiencies measured by Li et al. [24] in tests with 43−63 μm coal particles impacting a deposition plate in a laminar EFG at different carbon conversions are reported in Figure 12 for comparison. The capture efficiency was fairly small for coal conversion smaller than a threshold value (around 88%), whereas it sharply increased for larger coal conversion. This behaviour is related to the transition from a porous char particle, in which the molten mineral matter is encapsulated by the refractory carbon matrix, to a particle in which the residual carbon is

enclosed by the mineral slag. As a consequence, for coal conversion larger than about 90%, the particles become sticky and the capture efficiency sharply increases. The close resemblance of the two plots in Figure 12 suggests the usefulness of the physical modelling tool to characterize the *NSP→SP* transition occurring in realistic conditions by experiments with wax impacted at near-ambient conditions.

Figure 13 reports the effect of the temperature on both the global and normal coefficients of restitution. Results show that both ε_n and ε_g are constant, as the temperature increases from 20°C to 55°C, whereas at higher temperatures both the restitution coefficients decrease, becoming vanishingly small at 105°C. These experimental results are in agreement with those reported in Figure 12. Furthermore, these results suggest that ε_n, ε_t and ε_g to be used as boundary conditions in CFD codes should not be set as constant values, but rather as decreasing functions of temperature and carbon content of the fuel particle.

4.3. Rebound characteristics in the SP–NSW regime.

Figure 14 reports capture efficiency for droplets of 120±20 μm size upon collision against the Pyrex target at 120°C, while varying α_i and v_i. Capture efficiency is always larger than 85%, highlighting that deposition is by far the key phenomenon occurring for such impact experiments. At small values of α_i, capture efficiency slightly decreases with increasing impact velocities. This result can be explained by taking into account sliding and slipping phenomena [57], occurring more frequently at larger velocities. On the other hand, at large impact angles, this capture efficiency slightly increased with the incident velocity, as at larger impact velocities the viscous dissipation overtakes the inertial energy [57]. It is possible to conclude that, in the *SP–NSW* regime, the coefficients of restitution are zero while varying impact angles and velocities in the ranges investigated.

5. Conclusions.

The impact-deposition-rebound dynamical patterns of particles colliding with a planar surface have been investigated using high speed imaging and particle tracking. Experiments were carried out using montan wax particles whose solid/plastic versus fluid behaviour could be tuned by setting the temperature.

This experiment was used as a physical model to simulate and gain useful insight on the micromechanics of particle–wall interaction relevant to entrained-flow gasification of coal.

Increasing the particle temperature, particle–wall interaction shifted from prevailing rebound to deposition. In particular, the coefficients of restitution sharply decreased to zero when the particle temperature approached the incipient melting temperature, and a transition from “non sticky particle” to “sticky particle” occurred. Results obtained in the “non sticky wall–non sticky particle” regime indicate that coefficients of restitution are well below unity, as a consequence of plastic behaviour of the impacting particle. Coefficients of restitution are affected by impact angle, velocity and nature of the target materials. A significant decrease of the restitution coefficients was observed when particles were impacted against a powder-covered target, as a consequence of larger energy dissipation. These conditions favour the establishment of a segregation–coverage regime in a slagging entrained-flow gasifier, with the formation of a dense-dispersed phase in the near-wall reactor zone.

Acknowledgments.

The present study has been carried out in the framework of the project: “Ricerca di Sistema - Accordo MiSE-CNR Gruppo Tematico Carbone Pulito - Fondo per il Finanziamento Attività di Ricerca e Sviluppo di Interesse Generale per il Sistema Elettrico Nazionale”. The Authors wish to express their gratitude to Völpker Spezialprodukte GmbH (Germany), for supplying the wax Waradur E™. Furthermore, the Authors would like to acknowledge Miss Laura Pirro for the support in the experimental campaign and in the data analysis, Dr. Rossana Pasquino (UniNa) for the assessment of the rheological properties of the syrup, Dr. Pietro Russo (ICTP-CNR) and Dr. Massimo Lombardo (UniNa) for the mechanical characterization of the wax, and Dr. Piero Bareschino (Università del Sannio) for the assistance in the operation of the CCD camera and image postprocessing.

Nomenclature.

c constant [–]
C.E. capture efficiency [–]

d diameter [m]
E elastic modulus [Pa]
f momentum ratio [–]
G shear modulus [Pa]
K composite elastic modulus [Pa]
k stiffness ratio [–]
L eductor tube length [m]
N number [–]
p_y cut-off pressure [Pa]
Q volumetric flow rate [$m^3\ h^{-1}$]
T temperature [°C]
t time [s]
v velocity [$m\ s^{-1}$]
x parallel-to-wall coordinate [m]
X_C fractional conversion of carbon [–]
y normal-to-wall coordinate [m]

Greek Symbols.

α angle [°]
Γ surface energy [$N\ m^{-1}$]
γ surface tension [$N\ m^{-1}$]
ε coefficient of restitution [–]
μ viscosity [Pa s]
ν Poisson's ratio [–]
ρ density [$kg\ m^{-3}$]
σ stress [Pa]
τ particle relaxation time [s]

Subscripts.

1 referred to the particle
2 referred to the surface
a air
g global
i impact
n normal
p particle
r rebound
s sticking
syr syrup
t tangential
y yield

Superscripts.

* dimensionless
0 initial time
cr critical
tot total

References.

[1] T. Shimizu, H. Tominaga, A model of char capture by molten slag surface under high-temperature gasification conditions, Fuel 85 (2006) 170–178.

[2] T. Melchior, M. Bläsing, G. Pütz, M. Müller, Surface tension measurements of coal ash slags under reducing conditions at elevated pressures, Fuel 90 (2011) 280–287.

[3] J. Ni, G. Yu, Q. Guo, Z. Zhou, F. Wang, Submodel for predicting slag deposition formation in slagging gasification systems, Energy Fuel. 25 (2011) 1004–1009.

[4] W. Song, Y. Sun, Y. Wu, Z. Zhu, S. Koyama, Measurement and simulation of flow properties of coal ash slag in coal gasification, AIChE J. 57 (2011) 801–818.

[5] C. Higman, S. Tam, Advances in coal gasification, hydrogenation, and gas treating for the production of chemicals and fuels, Chem. Rev. 114 (2013) 1673–1708.

[6] J. Wang, H. Liu, Q. Liang, J. Xu, Experimental and numerical study on slag deposition and growth at the slag tap hole region of Shell gasifier, Fuel Process. Technol. 106 (2013) 704–711.

[7] G.N. Shannon, P.L. Rozelle, S.V. Pisupati, S. Sridhar, Conditions for entrainment into a FeO_X containing slag for a carbon-containing particle in an entrained coal gasifier, Fuel Process. Technol. 89 (2008) 1379–1385.

[8] S. Li, K.J. Whitty, Physical phenomena of char-slag transition in pulverized coal gasification, Fuel Process. Technol. 95 (2012) 127–136.

[9] M. Losurdo, H. Spliethoff, J. Kiel, Ash deposition modeling using a visco-elastic approach, Fuel 102 (2012) 145–155.

[10] L. Chen, S.Z. Yong, A.F. Ghoniem, Modeling the slag behavior in three dimensional CFD simulation of a vertically-oriented oxy-coal combustor, Fuel Process. Technol. 112 (2013) 106–117.

[11] F. Montagnaro, P. Salatino, Analysis of char-slag interaction and near-wall particle segregation in entrained-flow gasification of coal, Combust. Flame 157 (2010) 874–883.

[12] A. Slezak, J.M. Kuhlman, L.J. Shadle, J. Spenik, S. Shi, CFD simulation of entrained-flow coal gasification: coal particle density/size fraction effects, Powder Technol. 203 (2010) 98–108.

[13] F. Montagnaro, P. Brachi, P. Salatino, Char-wall interaction and properties of slag waste in entrained-flow gasification of coal, Energy Fuel. 25 (2011) 3671–3677.

[14] F. Ambrosino, A. Aprovitola, P. Brachi, F.S. Marra, F. Montagnaro, P. Salatino, Investigation of char-slag interaction regimes in entrained-flow gasifiers: linking experiments with numerical simulations, Combust. Sci. Technol. 184 (2012) 871–887.

[15] F. Ambrosino, A. Aprovitola, P. Brachi, F.S. Marra, F. Montagnaro, P. Salatino, Entrained-flow gasification of coal under slagging conditions: relevance of fuel-wall interaction and char segregation to the properties of solid wastes, Fuel 114 (2013) 44–55.

[16] S.Z. Yong, M. Gazzino, A. Ghoniem, Modeling the slag layer in solid fuel gasification and combustion – Formulation and sensitivity analysis, Fuel 92 (2012) 162–170.

[17] M. Troiano, R. Carbone, F. Montagnaro, P. Salatino, R. Solimene, A lab-scale cold flow model reactor to investigate near-wall particle segregation relevant to entrained-flow slagging coal gasifiers, Fuel 117 (2014) 1267–1273.

[18] M. Troiano, P. Salatino, R. Solimene, F. Montagnaro, Wall effects in entrained particle-laden flows: the role of particle stickiness on solid segregation and build-up of wall deposits, Powder Technol. 266 (2014) 282–291.

[19] L.L. Baxter, Ash deposition during biomass and coal combustion: a mechanistic approach, Biomass Bioenerg. 4 (1993) 85–102.

[20] L.L. Baxter, R.W. Desollar, A mechanistic description of ash deposition during pulverized coal combustion: predictions compared with observations, Fuel 72 (1993) 1411–1418.

[21] P. Isaak, H.N. Tran, D. Barham, D.W. Reeve, Stickiness of fireside deposits in kraft recovery units, J. Pulp Pap. Sci. 12 (1986) 84–88.

[22] H.N. Tran, X. Mao, D.C.S. Kuhn, R. Backman, M. Hupa, The sticky temperature of recovery boiler fireside deposits, Pulp Pap.-Can. 103 (2002) 29–33.

[23] L.E. Bool, S.A. Johnson, Effect of residual carbon on ash deposition behavior, American Society of Mechanical Engineers, Environmental Control Division Publication, EC 1 (1995) 305–312.

[24] S. Li, Y. Wu, K.J. Whitty, Ash deposition behavior during char-slag transition under simulated gasification condition, Energy Fuel. 24 (2010) 1868–1876.
[25] J.B. Kitto, S.C. Stultz, Steam, its generation and use, 41st Edition, The Babcock & Wilcox Company, Barberton, Ohio, U.S.A., 2005.
[26] J.C. van Dyk, F.B. Waanders, S.A. Benson, M.L. Laumb, K. Hack, Viscosity predictions of the slag composition of gasified coal, utilizing FactSage equilibrium modelling, Fuel 88 (2009) 67–74.
[27] P. Wang, M. Massoudi, Slag behavior in gasifiers. Part I: influence of coal properties and gasification conditions, Energies 6 (2013) 784–806.
[28] L.M. Gibson, N. Soundarrajan, J. Spenik, J. Ma, L. Shadle, S.V. Pisupati, Application of particle population model to determine the contribution to slag, flyash, and syngas in entrained flow gasification from particle size distribution, Energy Fuel. 27 (2013) 7681–7695.
[29] M. Dong, S. Li, J. Xie, J. Han, Experimental studies on the normal impact of fly ash particles with planar surfaces, Energies 6 (2013) 3245–3262.
[30] L.M. Gibson, B. Gopalan, S.V. Pisupati, L.J. Shadle, Image analysis measurements of particle coefficient of restitution for coal gasification applications, Powder Technol. 247 (2013) 30–43.
[31] H. Hertz, On the contact of elastic solids, Miscellaneous Papers by H. Hertz, Eds. D.E. Jones, and G.A. Schott, Macmillan, London, 146–162 (1896).
[32] K.L. Johnson, K. Kendall, A.D. Roberts, Surface energy and the contact of elastic solids, P. Roy. Soc. A-Math. Phy. 324 (1971) 301–313.
[33] L.N. Rogers, J. Reed, The adhesion of particles undergoing an elastic-plastic impact with a surface, J. Phys. D Appl. Phys. 17 (1984) 677–689.
[34] A.S. Yigit, A.P. Christoforou, M.A. Majeed, A nonlinear visco-elastoplastic impact model and the coefficient of restitution, Nonlinear Dynam. 66 (2011) 509–521.
[35] K.A. Ismail, W.J. Stronge, Viscoplastic analysis for direct impact of sports balls, Int. J. Nonlinear Mech. 47 (2012) 16–21.
[36] C. Thornton, Z. Ning, A theoretical model for the stick/bounce behaviour of adhesive, elastic-plastic spheres, Powder Technol. 99 (1998) 154–162.
[37] S. Wall, W. John, H.C. Wang, S.L. Goren, Measurements of kinetic energy loss for particles impacting surfaces, Aerosol Sci. Technol. 12 (1990) 926–946.
[38] R.M. Brach, P.F. Dunn, Models of rebound and capture for oblique microparticle impacts, Aerosol Sci. Technol. 29 (1998) 379–388.
[39] D.A. Gorham, A.H. Kharaz, The measurement of particle rebound characteristics, Powder Technol. 112 (2000) 193–202.
[40] C.Y. Wu, C. Thornton, L.Y. Li, Coefficients of restitution for elastoplastic oblique impacts, Adv. Powder Technol. 14 (2003) 435–448.
[41] C.Y. Wu, C. Thornton, L.Y. Li, A semi-analytical model for oblique impacts of elastoplastic spheres, P. Roy. Soc. A-Math. Phy. 465 (2009) 937–960.
[42] N. Maw, J.R. Barber, J.N. Fawcett, The role of elastic tangential compliance in oblique impact, J. Lubr. Technol. 103 (1981) 74–80.
[43] R. Li, N. Ashgriz, S. Chandra, J.R. Andrews, Shape and surface texture of molten droplets deposited on cold surfaces, Surf. Coat. Technol. 202 (2008) 3960–3966.
[44] D.W. Hobbs, The strength and the stress–strain characteristics of coal in triaxial compression, J. Geol. 72 (1964) 214–231.
[45] S. Zhong, F. Baitalow, P. Nikrityuk, H. Gutte, B. Meyer, The effect of particle size on the strength parameters of German brown coal and its chars, Fuel 125 (2014) 200–205.
[46] M. Massoudi, P. Wang, Slag behavior in gasifiers. Part II: constitutive modeling of slag, Energies 6 (2013) 807–838.
[47] G.P. Broom, Adhesion of particles in fibrous air filters, Filtr. Separat. 16 (1979) 661–669.
[48] H. Brauer, Report on investigations on particle movement in straight horizontal tubes, particle/wall collision and erosion of tubes and tube bends, J. Powder Bulk Solids Technol. 4 (1980) 3–12.
[49] M. Sommerfeld, N. Huber, Experimental analysis and modelling of particle-wall collisions, Int. J. Multiphas. Flow 25 (1999) 1457–1489.

[50] D. Tabor, A simple theory of static and dynamic hardness, Proc. Roy. Soc. Lond. 192 (1948) 247–274.
[51] A.B. Stevens, C.M. Hrenya, Comparison of soft-sphere models to measurements of collision properties during normal impacts, Powder Technol. 154 (2005) 99–109.
[52] O.V. Kim, P.F. Dunn, A microsphere-surface impact model for implementation in computational fluid dynamics, J. Aerosol Sci. 38 (2007) 532–549.
[53] H. Li, W.G. Jiang, X.Q. Feng, Normal impact of adhesive microparticles with a film/substrate system: a numerical study, Comput. Mater. Sci. 60 (2012) 130–136.
[54] M.C. van Beek, C.C.M. Rindt, J.G. Wijers, A.A. van Steenhoven, Rebound characteristics for 50-µm particles impacting a powdery deposit, Powder Technol. 165 (2006) 53–64.
[55] M.S. Abd-Elhady, C.C.M. Rindt, J.G. Wijers, A.A. van Steenhoven, Modeling the impaction of a micron particle with a powdery layer, Powder Technol. 168 (2006) 111–124.
[56] R.G. Craig, J.D. Eick, F.A. Peyton, Properties of natural waxes used in dentistry, J. Dent. Res. 44 (1965) 1308–1316.
[57] S. Sikalo, E.N. Ganic, Phenomena of droplet-surface interactions, Exp. Therm. Fluid Sci. 31 (2006) 97−110.

Table 1. Mechanical properties of montan wax Waradur E and of different reference coals and slag.

Material	Young modulus, E (MPa)	Strength, (MPa)
Waradur E wax	700±66	9.5±2.5[a]
Coal (Rank Code No. 100a)	3675±545	17±2.82[b]
Coal (Rank Code No. 201)	1324±193	5.3±0.83[b]
Coal (Rank Code No. 301)	400±103	1.93±0.27[b]
Coal (Rank Code No. 801)	3805±41.37	26.54±2.07[b]
Schleenhain brown coal	43±15	2.35±0.78[c]
Schleenhain brown coal char obtained at 800 °C	206±63	11.2±5[c]
Slag (at 1000°C and 1450°C)[d]	20000–5000	

[a] 0.2% offset yield strength.
[b] After [44], yield strength.
[c] After [45], compressive strength.
[d] Calculated after [46].

Table 2. Surface energies of target materials.

	Pyrex	Stainless steel	Wax	Teflon
Surface energy, Γ (N m^{-1})	1	0.8	0.03	0.02

Table 3. Operating test parameters.

	NSP–NSW	*NSP→SP* transition	*SP–NSW*
Air temperature, T_a (°C)	20	20–110	120
Air flow rate, Q_a ($m^3\ h^{-1}$ @273 K)	2–8	3–4	3–5
Particle diameter, d_p (µm)	75±10	80±15	120±20
Impact velocity, v_i ($m\ s^{-1}$)	0.5–3	2	0.7–5
Impact angle, α_i (°)	10–90	84±4	15–90
Target material	• Pyrex • Stainless steel • Montan wax Waradur E • Teflon	Pyrex	Pyrex
Target surface properties	• Flat polished surface • Surface covered with 0.25 mm-thick layer of powdered wax • Surface covered with 1.4 mm-thick layer of powdered wax • Surface covered with syrup and 0.2 mm-thick layer of powdered wax	–	–

Table 4. Mechanical properties of the reference target materials, and values of critical velocities (obtained by Eqs. (1), (3)). Operating conditions: *NSP–NSW* regime (T_a=20°C).

Target material	Γ (N m^{-1})	E (GPa)	ν (–)	v_y (m s^{-1})	v_s (m s^{-1})
Teflon	0.02	0.50	0.46	$6.8 \cdot 10^{-3}$	$3.02 \cdot 10^{-2}$
Wax	0.03	0.70	0.49	$6.8 \cdot 10^{-3}$	$3.03 \cdot 10^{-2}$
Stainless Steel	0.80	190	0.30	$6.8 \cdot 10^{-3}$	$1.04 \cdot 10^{-2}$
Pyrex	1	64	0.20	$6.8 \cdot 10^{-3}$	$1.15 \cdot 10^{-2}$

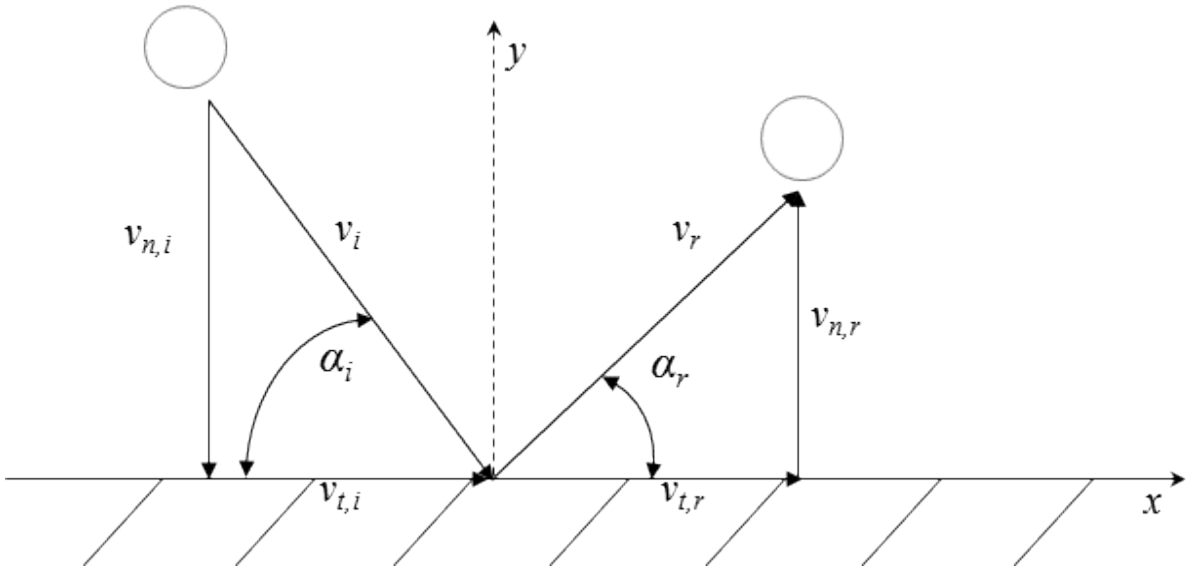

Figure 1. Outline of particle impact with a planar surface.

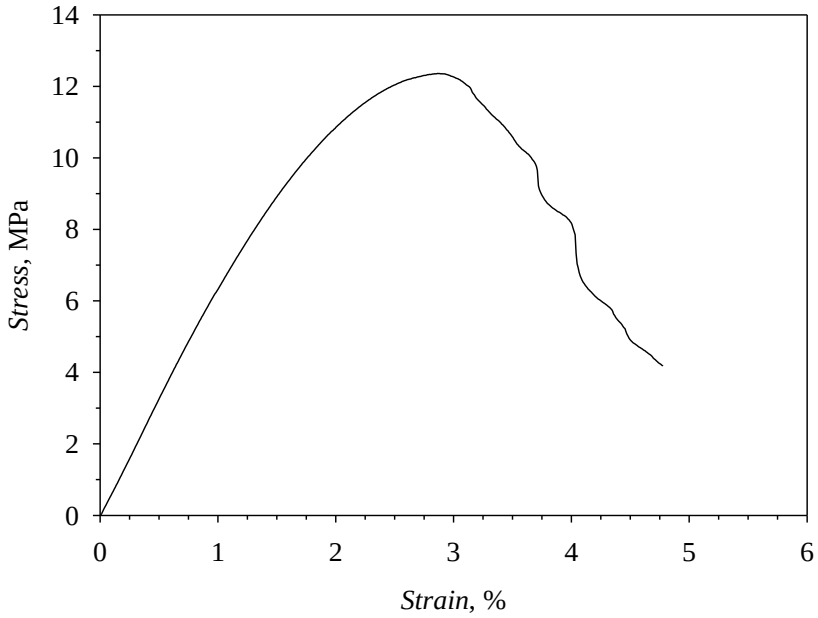

Figure 2. Typical stress–strain curve for wax samples.

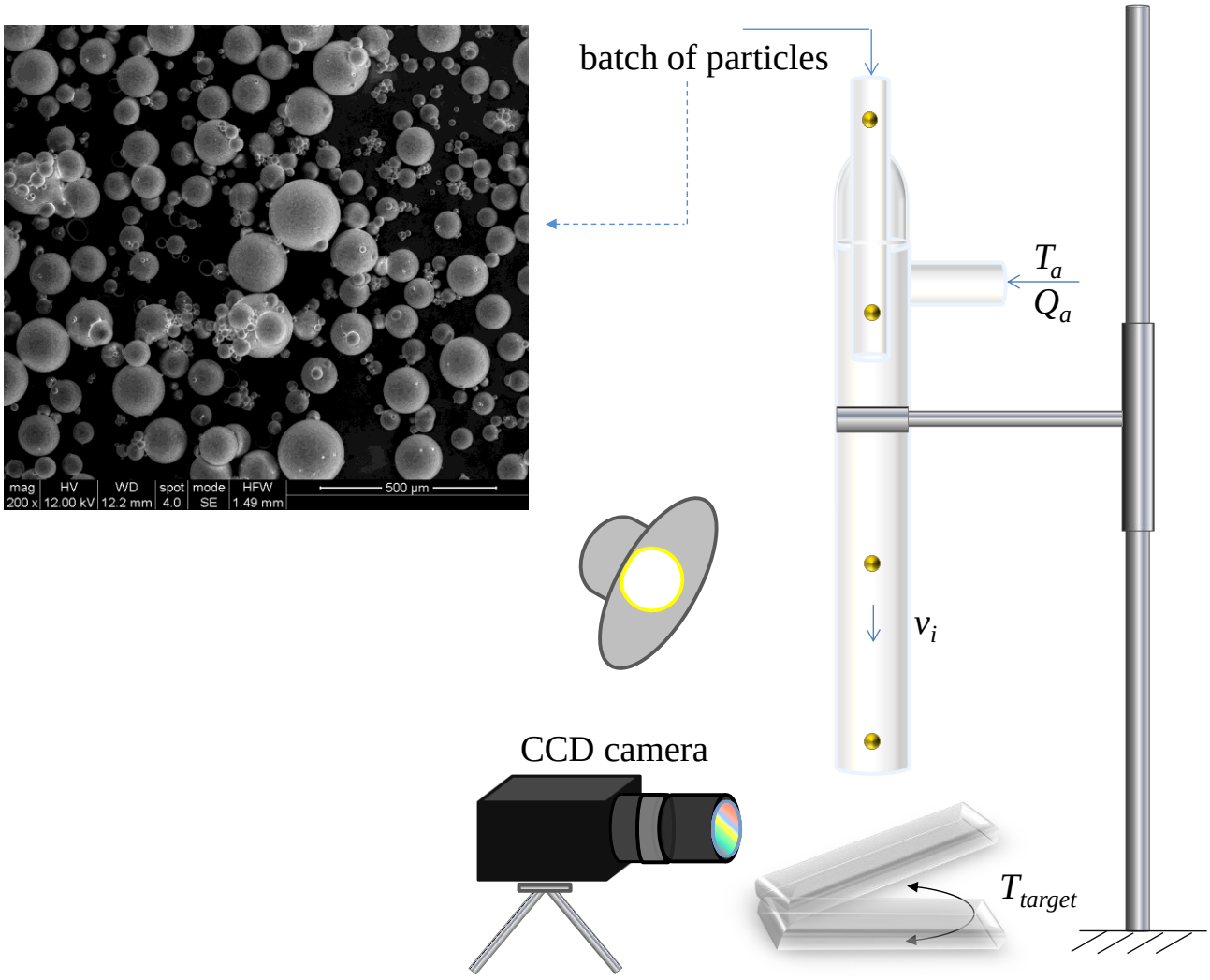

Figure 3. Outline of the particle–wall impact apparatus. Inset: SEM micrograph of a wax particles sample.

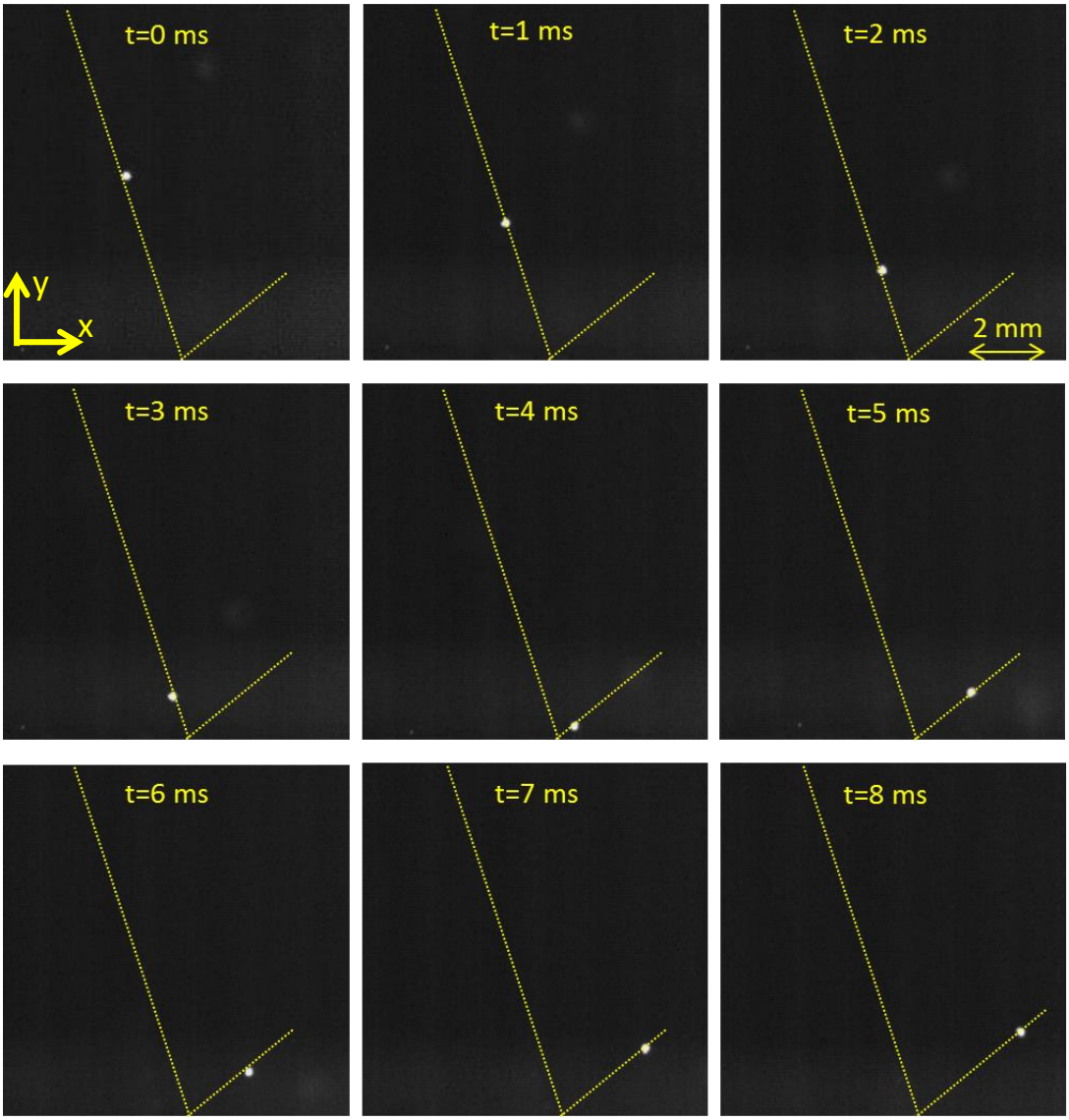

Figure 4. Snapshots captured during a typical particle impact (d_p=70 μm). Dotted lines represent the particle trajectory before and after the collision.

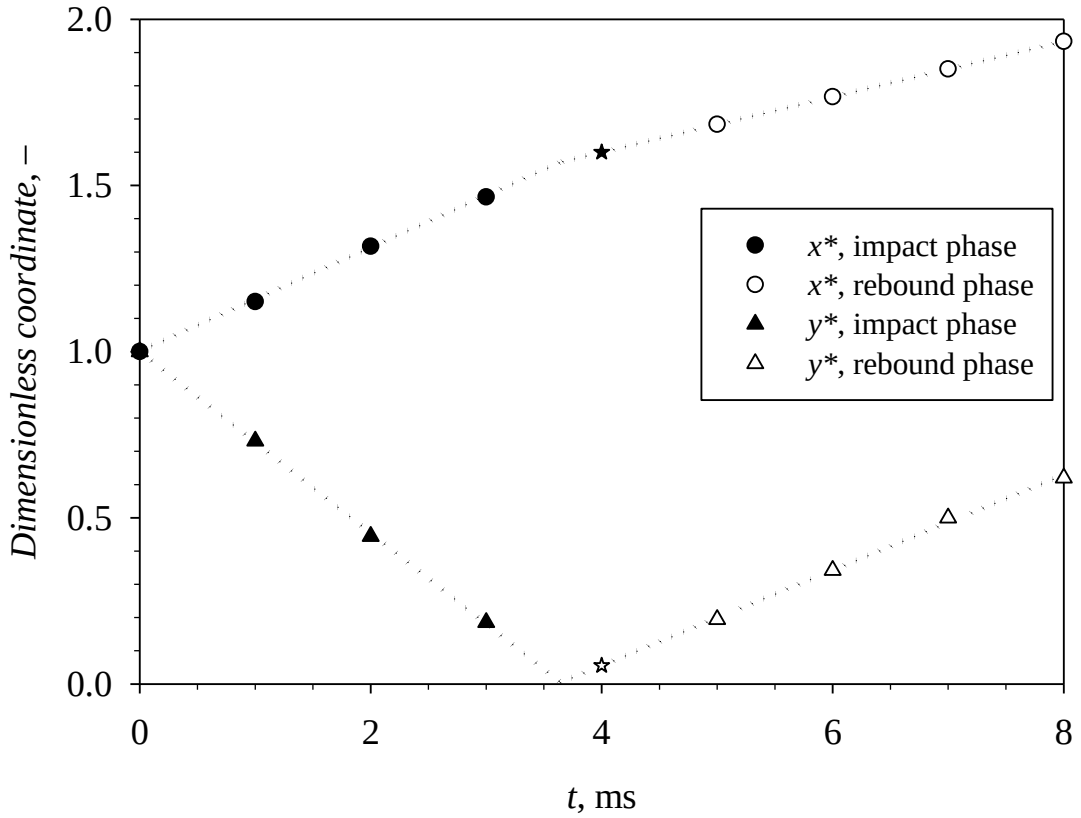

Figure 5. Time-series of the particle dimensionless coordinates, x^* and y^*, before/after impact for the sample test reported in Figure 4. The star marks the time (t=4 ms) corresponding to the closest particle position to the target.

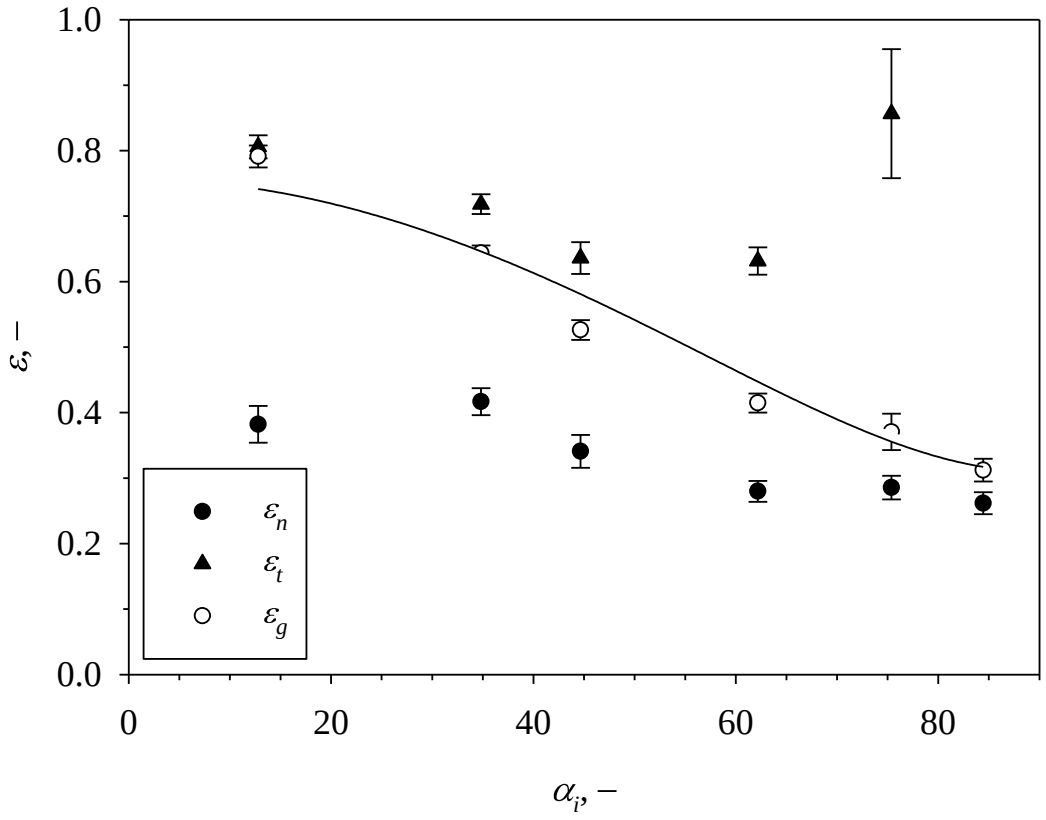

Figure 6. Effect of the impact angle on the coefficients of restitution. The line represents the fitting of the ε_g experimental data points by using Eq. (9). Operating conditions: *NSP–NSW* regime (T_a=20°C), v_i=1 m s^{-1}, Pyrex target.

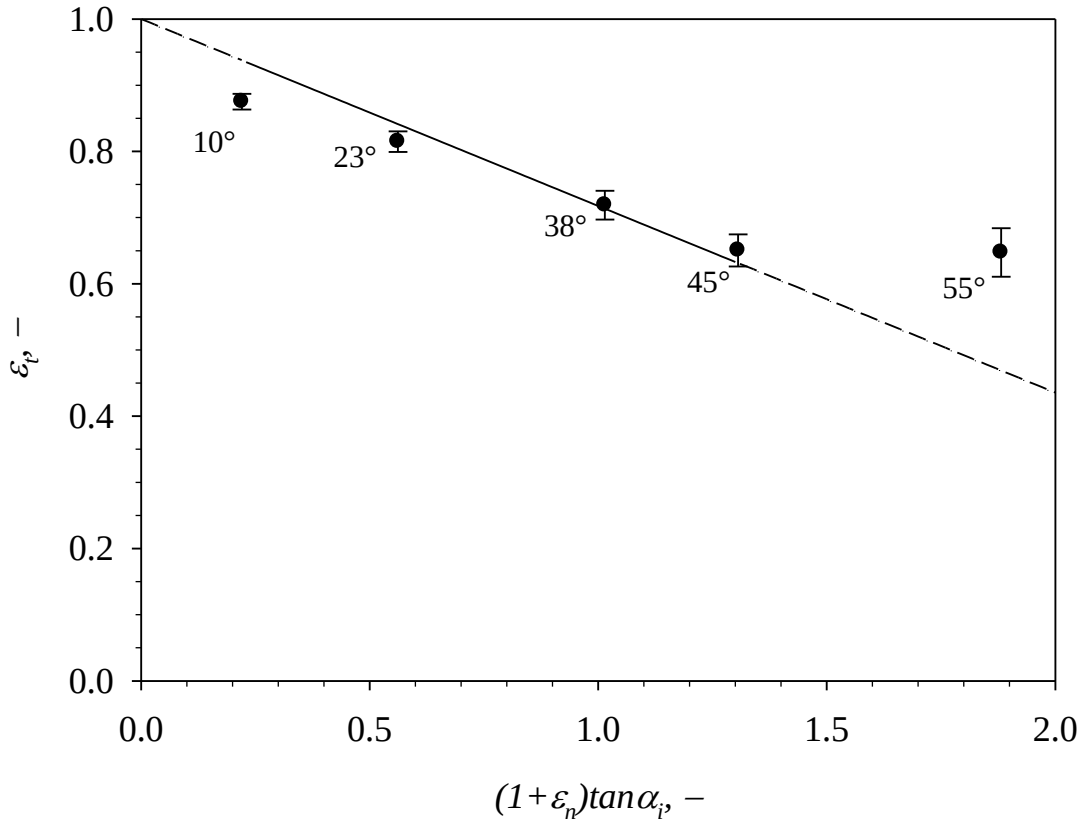

Figure 7. Tangential coefficient of restitution: plot based on Eq. (10). Symbols represent experimental data points; the solid line represents the linear data fitting for impact angles between 10° and 45°. Operating conditions: *NSP–NSW* regime (T_a=20°C), v_i=1 m s^{-1}, Pyrex target.

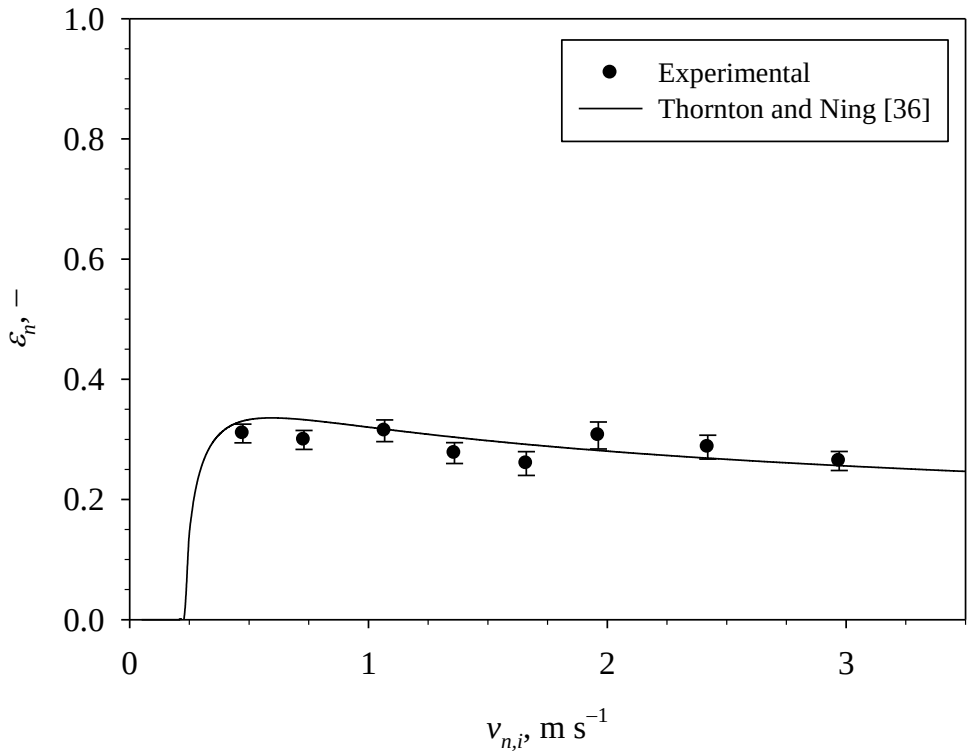

Figure 8. Effect of the normal impact velocity on normal coefficient of restitution. Operating conditions: *NSP–NSW* regime (T_a=20°C), α_i=84°, Pyrex target.

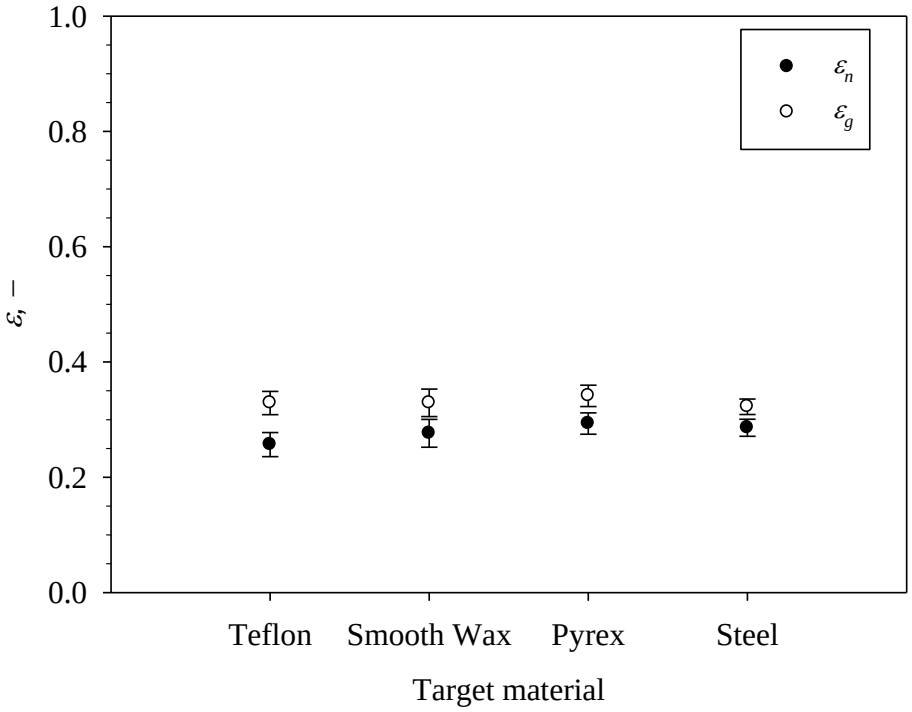

Figure 9. Effect of the target material on normal and global coefficient of restitution. Operating conditions: *NSP–NSW* regime (T_a=20°C), v_i=1.25 m s^{-1}, α_i=84°.

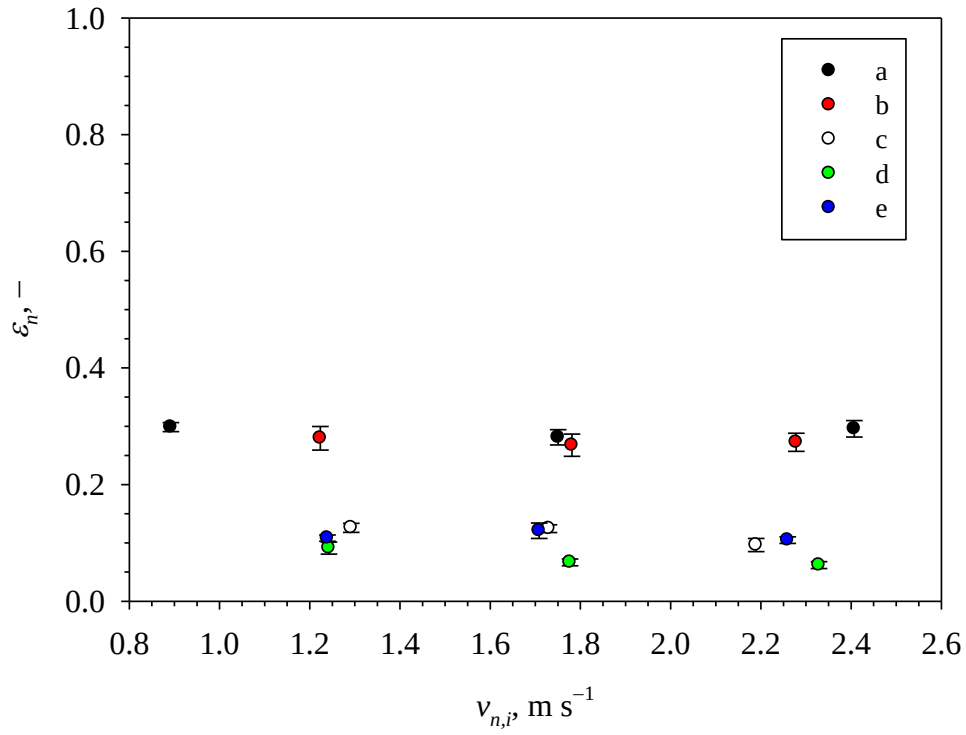

Figure 10. Effect of target surface on normal coefficient of restitution. Operating conditions: *NSP–NSW* regime (T_a=20°C), α_i=84°. Key to symbols: a) Pyrex; b) Wax, smooth surface; c) Pyrex surface covered with 0.25 mm-thick layer of powdered wax; d) Surface covered with 1.4 mm-thick layer of powdered wax; e) Surface covered with syrup and 0.2 mm-thick layer of powdered wax.

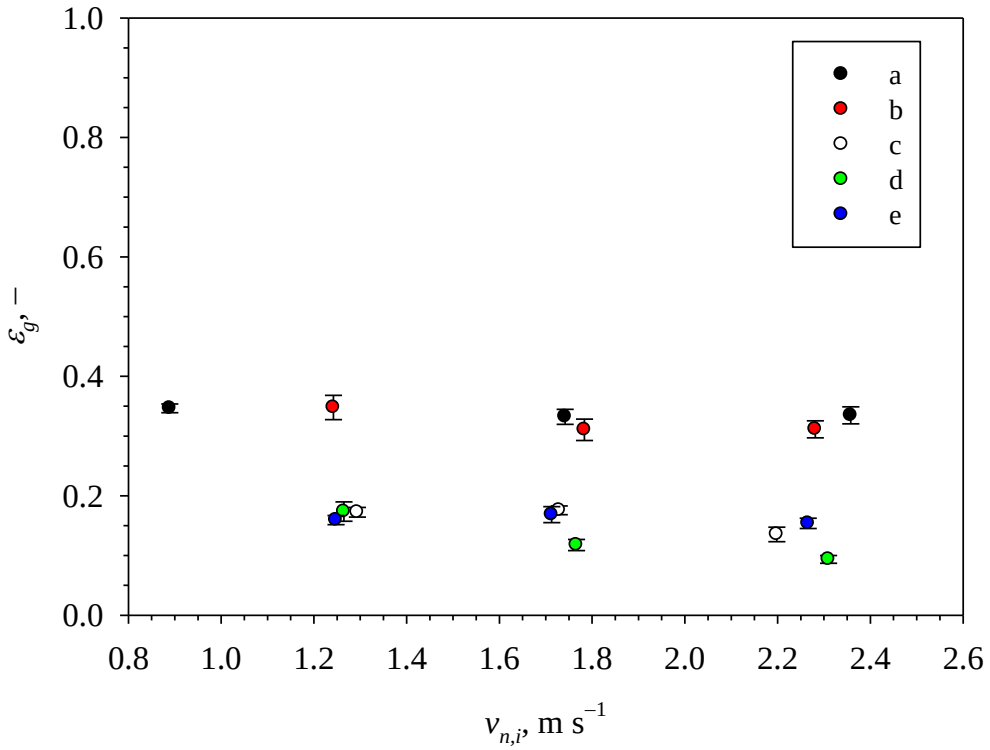

Figure 11. Effect of target surface on global coefficient of restitution. Operating conditions: *NSP–NSW* regime (T_a=20°C), α_i=84°. Key to symbols: a) Pyrex; b) Wax, smooth surface; c) Pyrex surface covered with 0.25 mm-thick layer of powdered wax; d) Surface covered with 1.4 mm-thick layer of powdered wax; e) Surface covered with syrup and 0.2 mm-thick layer of powdered wax.

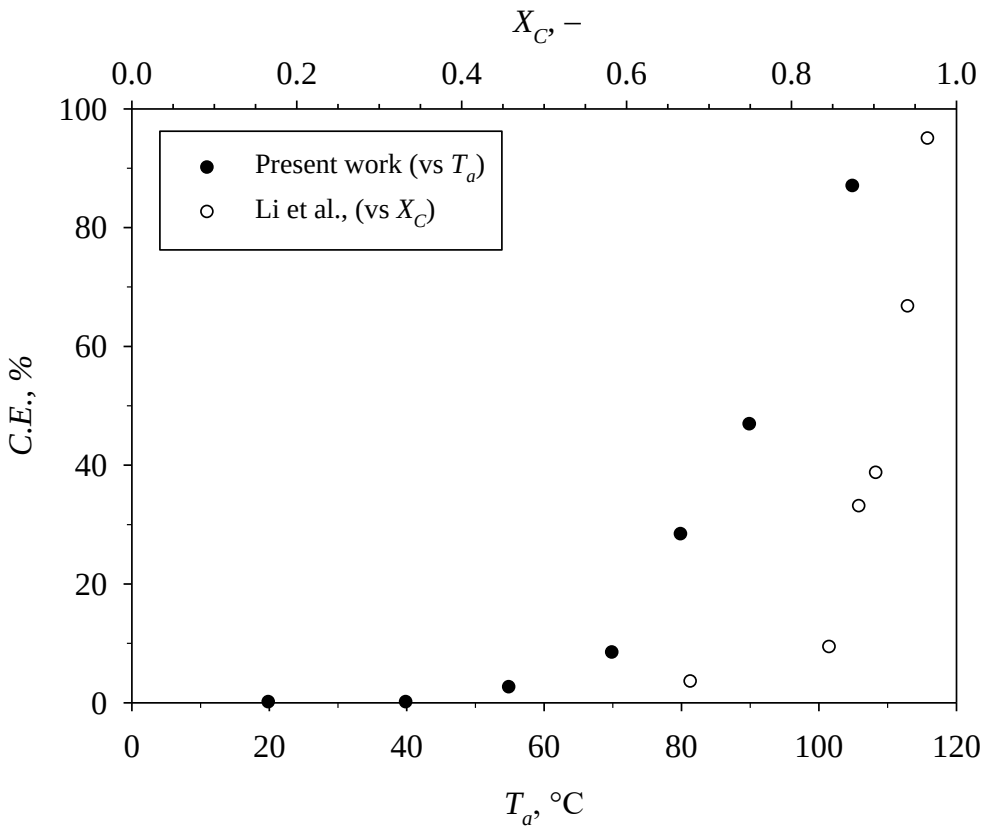

Figure 12. Effect of the particle temperature (present study) and of the fractional carbon conversion (after [24]) on particle capture efficiency. Operating conditions: *NSW* and *NSP→SP* transition, v_i=2 m s^{-1}, α_i=84°, Pyrex target.

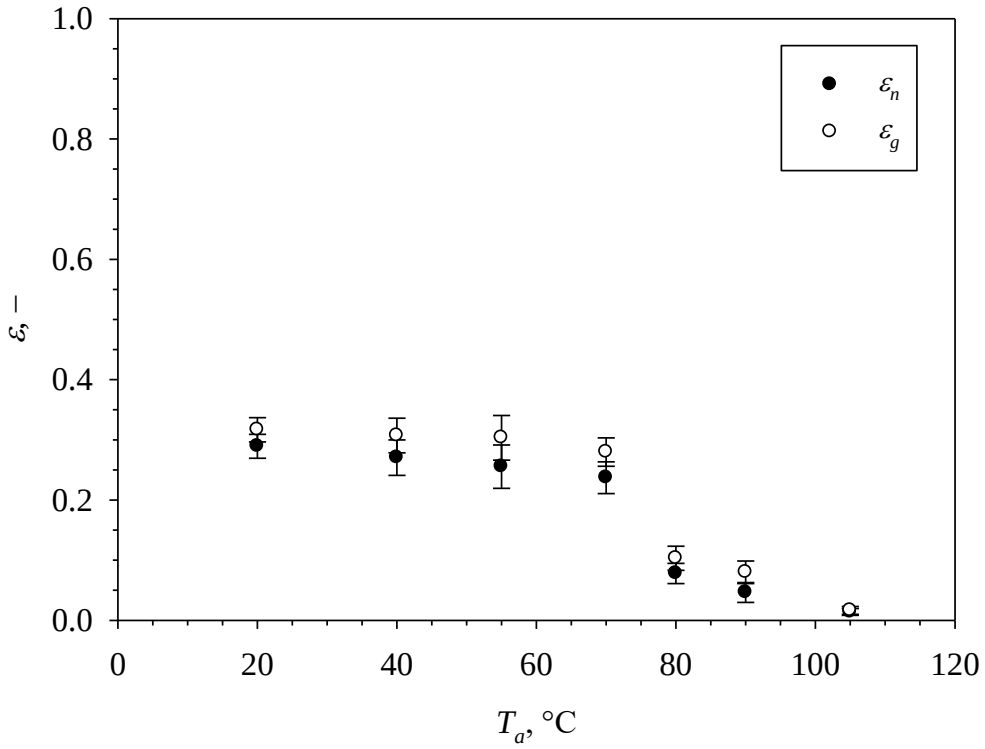

Figure 13. Effect of particle temperature on normal and global coefficients of restitution. Operating conditions: *NSW* and *NSP→SP* transition, v_i=2 m s^{-1}, α_i=84°, Pyrex target.

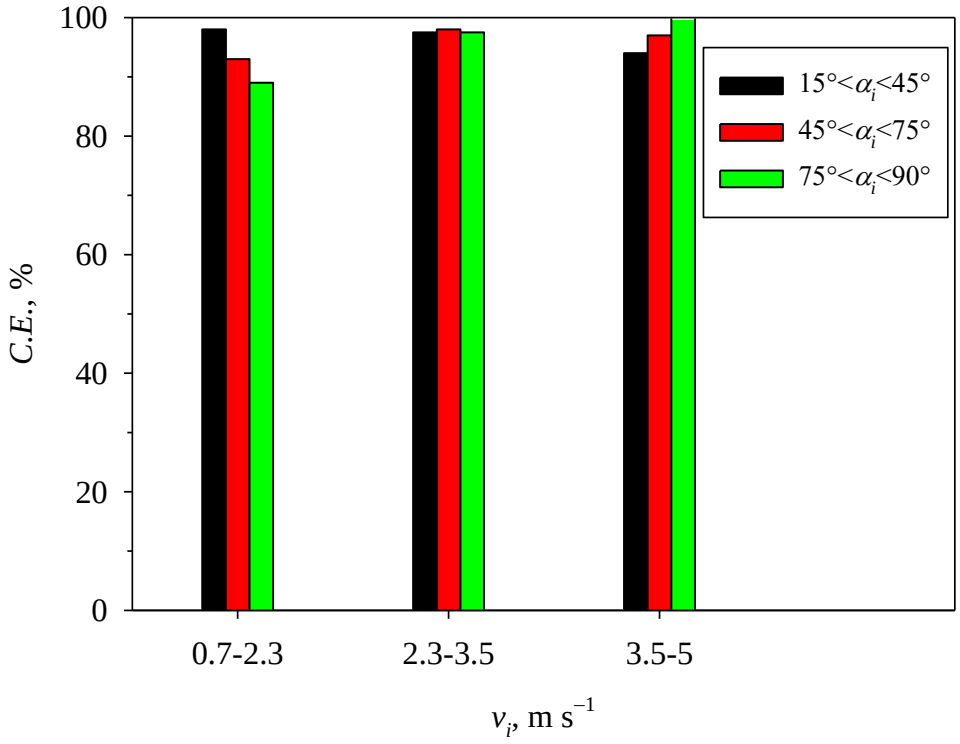

Figure 14. Effect of the impact angle and impact velocity on particle capture efficiency in the *SP–NSW* regime. Operating conditions: T_a=120°C, Pyrex target.